



ELSEVIER

Available online at www.sciencedirect.com

SCIENCE @ DIRECT®

Journal of Computational Physics 210 (2005) 608–631

JOURNAL OF
COMPUTATIONAL
PHYSICS

www.elsevier.com/locate/jcp

Artificial compressibility, characteristics-based schemes for variable-density, incompressible, multispecies flows: Part II. Multigrid implementation and numerical tests

Evgeniy Shapiro, Dimitris Drikakis *

Fluid Mechanics and Computational Science Group, School of Engineering, Cranfield University, Cranfield, Bedfordshire MK43 0AL, United Kingdom

Received 10 January 2005; received in revised form 29 April 2005; accepted 3 May 2005
Available online 11 July 2005

Abstract

The paper presents an investigation of the accuracy and efficiency of artificial compressibility, characteristics-based (CB) schemes for variable-density incompressible flows. The CB schemes have been implemented in conjunction with a multigrid method for accelerating numerical convergence and a fourth-order, explicit Runge–Kutta method for the integration of the governing equations in time. The implementation of the CB schemes is obtained in conjunction with first-, second- and third-order interpolation formulas for calculating the variables at the cell faces of the computational volume. The accuracy and efficiency of the schemes are examined against analytical and experimental results for diffusion broadening in two- and three-dimensional microfluidic channels, a problem that has motivated the development of the present methods. Moreover, unsteady, inviscid simulations have been performed for variable-density mixing layer. The computations revealed that accuracy and efficiency depend on the CB scheme design. The best multigrid convergence rates were exhibited by the conservative CB scheme, which is obtained by the fully conservative formulation of the variable-density, incompressible equations.

© 2005 Elsevier Inc. All rights reserved.

MSC: 65C20; 76M20

Keywords: Variable-density flows; Artificial compressibility; Characteristics-based schemes; Multigrid; High-resolution schemes; Microfluidics; Mixing layer; Euler equations; Navier–Stokes equations

DOI of original article: [10.1016/j.jcp.2005.05.001](https://doi.org/10.1016/j.jcp.2005.05.001).

* Corresponding author. Tel.: +44 1234 754796; fax: +44 1234 758207.

E-mail address: d.drikakis@cranfield.ac.uk (D. Drikakis).

0021-9991/\$ - see front matter © 2005 Elsevier Inc. All rights reserved.
doi:10.1016/j.jcp.2005.05.002

1. Introduction

Even though there are a number of studies that have been concerned with the development of pressure projection methods for variable-density flows [1,2], the development of numerical methods for these flows in the framework of artificial compressibility has received scant attention in the literature. In [3], three numerical formulations for the governing equations for variable-density flows, all based on the artificial compressibility approach [4], were presented. On the basis of these formulations, characteristics-based schemes were derived along similar lines as for compressible [5] and constant-density incompressible flows [6,7]. The variants of CB schemes derived in [3], labeled as *transport*, *conservative* and *hybrid*, differed with respect to the formulation of the transport equation for total density and the use of divergence-free condition. The transport CB scheme reconstructs numerically species and total densities along the streamlines, while in the conservative CB scheme pseudo-compressibility terms are added into the reconstruction formulas for the density. Finally, the hybrid CB scheme reconstructs the densities along the streamlines, similar to the transport CB scheme, while the eigenvalues of the system of equations are the same with the eigenvalues of the conservative CB scheme.

In this paper, we present the numerical implementation of the artificial compressibility CB schemes in conjunction with multigrid techniques. Implementation of different variants of multigrid methods in conjunction with the artificial compressibility approach have been presented in the literature for computations of laminar flows [8,9], free surface flows (based on Euler simulations) [11], turbulent flows [12,13], incompressible low-Mach number flows [14], as well as using adaptive grids [9] and adaptive solvers [15]. Pertinent to the multigrid implementation for AC are also research works on multigrid methods for the preconditioned Euler/Navier–Stokes equations for low-Mach number, steady and unsteady flows [16–19]. The combination of multigrid methods and artificial compressibility in the context of different variable-density formulations has not been previously discussed in the literature, thus motivating a detailed numerical investigation. Therefore, numerical tests have been performed for three flow problems: (i) diffusion broadening in a two-dimensional microfluidic channel; (ii) diffusion broadening in a three-dimensional microfluidic channel; and (iii) time-dependent evolution of variable density mixing layer.

Microfluidics have been a research subject of increasing interest in the past few years, mainly because of the wide range of practical applications. Two-fluid laminar flow at low Reynolds numbers are extensively used in chemical separation, extraction and detection [20–23] as well as in microreactors [24], micromixing devices [25] and biotechnology [26]. An extensive review of microfluidic devices applications in biotechnology and organic chemistry can be found in [29]. Another important application of microfluidics is in microfabrication [28], where liquid interfaces are created by laminar flow in microfluidic channels. In all the above applications, the characteristic microchannel dimensions are of order $10^2 \mu\text{m}$ which is still in the domain of continuum mechanics simulations [27]. The Reynolds numbers occurring in these applications range from $Re \ll 1$ (flow sensors, heat sink channels, capillary tubes [35]), $Re \sim 10^{-1}–10^2$ (e.g., in diffusion broadening [31] and micromixers [34]) to $Re > 10^3$ (microvalves, micronozzles/pumps [35]).

When two miscible species are supplied via separated inlets into a channel with rectangular cross section they will result in the development of a diffusion front (see Fig. 1). This problem has been studied experimentally, analytically and numerically by a number of researchers. Ismagilov et al. [30] analyzed the advection–diffusion equations for a fully developed three-dimensional flow and indicated that the diffusion front position power-law dependency on the streamwise direction (i.e., along the channel) varies from 0.5 in the middle of the channel to $1/3$ near the channel wall. These results were found to be in agreement with both experimental data [30,31] as well as numerical solutions [31]. The latter were obtained by solving the Navier–Stokes equations for the flow field, which in turn is used to compute advection–diffusion equations for species transfer (decoupled solution). Other modeling approaches for diffusion broadening include decoupled two and three-dimensional solutions of advection–diffusion

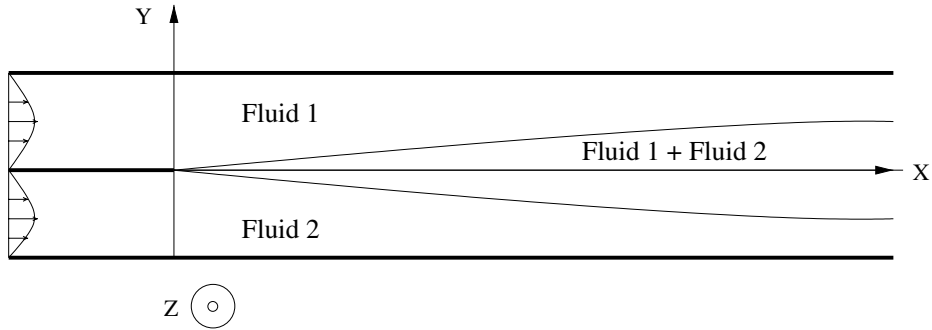


Fig. 1. Schematic of the diffusion broadening problem.

equations, simplifying the problem for the part of the channel that does not depend on the streamwise direction [32,33].

In this paper, the diffusion broadening problem has been employed at constant Peclet numbers and densities ratios and at different Reynolds numbers, in order to assess the accuracy and efficiency of the artificial-compressibility CB schemes. This includes investigation of the multigrid efficiency as well as different variations of intercell variable interpolation. Furthermore, an assessment of the accuracy and efficiency of the present methods has been carried out for variable-density temporal mixing-layer flow, which is initiated by a hyperbolic tangent velocity profile (see Fig. 2). This problem has been extensively studied for single fluid cases, including linear stability analysis [36], and has become an

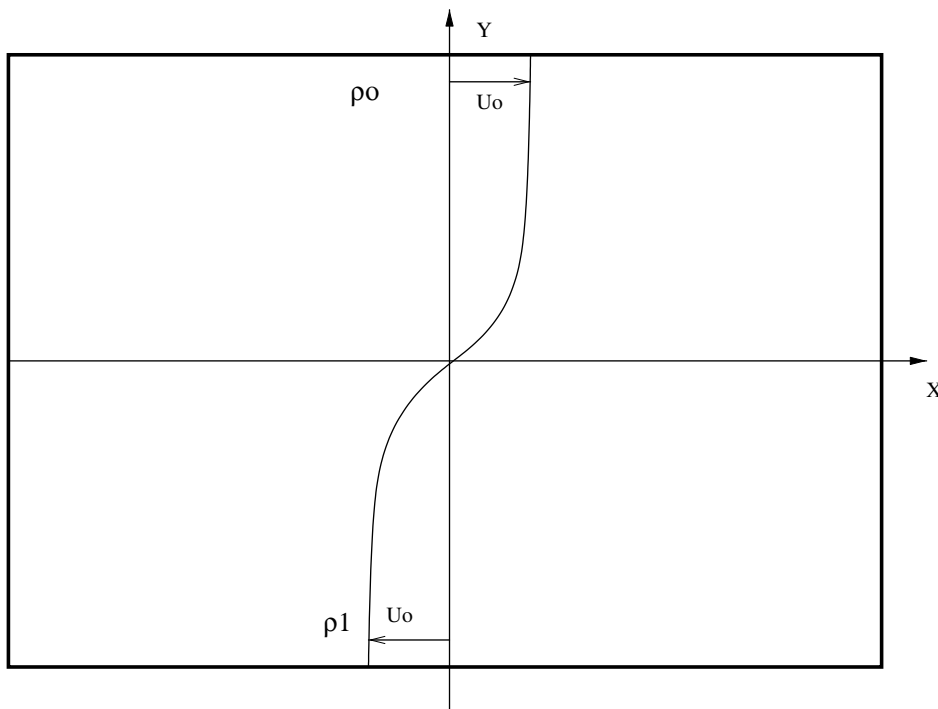


Fig. 2. Computational setup for the variable-density mixing layer problem.

established test bed for comparison of different numerical schemes [37–41]. A temporal (reacting) shear layer and the effect of non-uniform density on its development have been studied by Ghoniem et al. [43,44]. The effect of non-uniform liquid entrainment resulting in displacement of the vortex-center towards the lighter fluid has been observed in our computations and this is in accord with previous studies [44–47].

The paper is organized as follows. In Section 2, a summary of the three variable-density formulations and CB schemes used in this investigation is presented. Section 3 discusses the multigrid implementation of the artificial-compressibility CB schemes. Section 4 presents numerical results for the 2-D and 3-D diffusion broadening problems, while Section 5 presents results for the temporal variable-density mixing layer. Finally, Section 6 summarizes the main conclusions drawn from the present research.

2. Numerical formulation

Our numerical model comprises of the incompressible Navier–Stokes equations, the species transport equations for species densities and the artificial compressibility approach for coupling the continuity and momentum equations. The artificial-compressibility for steady flow problems adds a pseudo-time pressure derivative to the continuity equation [4]. For unsteady problems pseudo-time velocity derivatives need to be added to the momentum equations and for variable density problems pseudo-time density derivatives also need to be added to the densities transport equations. The pseudo-time velocity and densities derivatives are required for coupling and solving the governing equations in pseudo-time, τ . Based on the above, the non-dimensional system of equations is written as

$$\begin{cases} \frac{\partial \vec{u}}{\partial \tau} = -\frac{\partial \vec{u}}{\partial t} - \left((\vec{u} \cdot \nabla) \vec{u} + \frac{1}{\rho} \nabla p - \frac{1}{Re_l} \nabla^2 \vec{u} \right), \\ \frac{\partial p}{\partial \tau} = -\beta \nabla \cdot \vec{u}, \\ \frac{\partial \rho}{\partial \tau} = -\frac{\partial \rho}{\partial t} - (\vec{u} \cdot \nabla) \rho, \\ \frac{\partial \rho_i}{\partial \tau} = -\frac{\partial \rho_i}{\partial t} - \left((\vec{u} \cdot \nabla) \rho_i - \frac{1}{Pe} \nabla \cdot \left(\sum_{l=1}^{l=N-1} D_{li} \rho \nabla \frac{\rho_l}{\rho} \right) \right). \end{cases} \quad (1)$$

At each real time step, t , the solution of the system (1) is obtained by iterating in pseudo-time, τ , until convergence is achieved within a prescribed convergence tolerance; thus the incompressibility (divergence free) condition is satisfied at each time step. The parameters and variables in the above equations are defined as follows: b is the artificial compressibility parameter; \vec{u} is the velocity vector with components (u, v, w) for the three Cartesian directions (x, y, z) , respectively; q is the fluid density; p is the pressure; and $Re_l = U_0 L / m_l$ denotes the Reynolds number, where U_0 and L denote reference values for the velocity and spatial dimension, respectively, while m_l is the local kinematic viscosity. The partial densities are defined as q_i ($i = 1, N$) for a flow containing N species and the total density is defined by the sum of partial densities $q \equiv \sum q_i$. Further, $Pe = U_0 L / D$ and D_{li} stand for the Peclet number and (dimensionless) reduced multicomponent diffusion coefficients matrix, respectively, where D is a reference diffusion coefficient [48,49]. We write the system of equations in curvilinear coordinates

$$\frac{\partial \mathcal{J} \mathbf{U}}{\partial \tau} = -\frac{\partial \mathcal{J} \mathbf{U}_r}{\partial t} + \frac{\partial \mathbf{E}_v}{\partial \xi} + \frac{\partial \mathbf{F}_v}{\partial \eta} + \frac{\partial \mathbf{G}_v}{\partial \zeta} - \frac{\partial \mathbf{E}_i}{\partial \xi} - \frac{\partial \mathbf{F}_i}{\partial \eta} - \frac{\partial \mathbf{G}_i}{\partial \zeta} \equiv \mathbf{RHS}, \quad (2)$$

where $\mathbf{U} = (p/b, qu, qv, qw, q, q_i)^T$, $\mathbf{U}_r = (0, qu, qv, qw, q, q_k)^T$ and the inviscid, $(\mathbf{E}_i, \mathbf{F}_i, \mathbf{G}_i)$, and viscous, $(\mathbf{E}_v, \mathbf{F}_v, \mathbf{G}_v)$, fluxes are given by

$$\left\{ \begin{array}{l} \mathbf{E}_I = J \left(\mathbf{E}_I^c \frac{\partial \xi}{\partial x} + \mathbf{F}_I^c \frac{\partial \xi}{\partial y} + \mathbf{G}_I^c \frac{\partial \xi}{\partial z} \right), \\ \mathbf{F}_I = J \left(\mathbf{E}_I^c \frac{\partial \eta}{\partial x} + \mathbf{F}_I^c \frac{\partial \eta}{\partial y} + \mathbf{G}_I^c \frac{\partial \eta}{\partial z} \right), \\ \mathbf{G}_I = J \left(\mathbf{E}_I^c \frac{\partial \zeta}{\partial x} + \mathbf{F}_I^c \frac{\partial \zeta}{\partial y} + \mathbf{G}_I^c \frac{\partial \zeta}{\partial z} \right), \\ \mathbf{E}_V = J \left(\mathbf{E}_V^c \frac{\partial \xi}{\partial x} + \mathbf{F}_V^c \frac{\partial \xi}{\partial y} + \mathbf{G}_V^c \frac{\partial \xi}{\partial z} \right), \\ \mathbf{F}_V = J \left(\mathbf{E}_V^c \frac{\partial \eta}{\partial x} + \mathbf{F}_V^c \frac{\partial \eta}{\partial y} + \mathbf{G}_V^c \frac{\partial \eta}{\partial z} \right), \\ \mathbf{G}_V = J \left(\mathbf{E}_V^c \frac{\partial \zeta}{\partial x} + \mathbf{F}_V^c \frac{\partial \zeta}{\partial y} + \mathbf{G}_V^c \frac{\partial \zeta}{\partial z} \right). \end{array} \right. \quad (3)$$

The Cartesian inviscid ($\mathbf{E}_I^c, \mathbf{F}_I^c, \mathbf{G}_I^c$) and viscous ($\mathbf{E}_V^c, \mathbf{F}_V^c, \mathbf{G}_V^c$) fluxes are defined by

$$\left\{ \begin{array}{l} \mathbf{E}_I^c = (u, \rho u^2 + p, \rho uv, \rho uw, \rho u, \rho_i u)^T, \\ \mathbf{F}_I^c = (v, \rho uv, \rho v^2 + p, \rho vw, \rho v, \rho_i v)^T, \\ \mathbf{G}_I^c = (w, \rho uw, \rho vw, \rho w^2 + p, \rho w, \rho_i w)^T, \\ \mathbf{E}_V^c = \left(0, \tau_{xx}, \tau_{xy}, \tau_{xz}, 0, \frac{1}{Pe} \sum_{l=1}^{l=N-1} D_{li} \rho \frac{\partial \rho_l / \rho}{\partial x} \right)^T, \\ \mathbf{F}_V^c = \left(0, \tau_{yx}, \tau_{yy}, \tau_{yz}, 0, \frac{1}{Pe} \sum_{l=1}^{l=N-1} D_{li} \rho \frac{\partial \rho_l / \rho}{\partial y} \right)^T, \\ \mathbf{G}_V^c = \left(0, \tau_{zx}, \tau_{zy}, \tau_{zz}, 0, \frac{1}{Pe} \sum_{l=1}^{l=N-1} D_{li} \rho \frac{\partial \rho_l / \rho}{\partial z} \right)^T, \end{array} \right. \quad (4)$$

where τ_{ij} stand for the components of the viscous stress tensor. The discretization of the inviscid terms is obtained by characteristics-based schemes. These were derived in Part I [3], where it was shown that three different schemes can be obtained depending on the formulation of the governing equations. These formulations and the corresponding CB schemes are summarized below:

- *Transport CB scheme.* The equations for densities are written as advection equations¹ in non-conservative form and these are used to eliminate the total density from the momentum equations of the conservative system (2). The advective flux in, e.g., n -direction, is computed using the reconstructed primitive variables (denoted by ‘tilde’) defined by

$$\left\{ \begin{array}{l} \tilde{p} = \frac{1}{2s} (\lambda_1 p_2 - \lambda_2 p_1 - \beta(R_1 - R_2)), \\ \tilde{u} = u_0 + \frac{\tilde{x}}{2s\rho} R_3, \\ \tilde{v} = v_0 + \frac{\tilde{y}}{2s\rho} R_3, \\ \tilde{w} = w_0 + \frac{\tilde{z}}{2s\rho} R_3, \\ \tilde{\rho} = \rho_0, \\ \tilde{\rho}_i = \rho_{i0}, \\ i = 1, N - 1, \end{array} \right. \quad (5)$$

¹ Note that the CB schemes refer to the discretization of the advective fluxes.

where $s = \sqrt{\lambda_0^2 + \beta/\rho}$; the eigenvalues of the inviscid matrix \mathbf{E}_I are given by $\lambda_0 = u\tilde{x} + v\tilde{y} + w\tilde{z}$ ($N - 1$ eigenvalues), $k_1 = k_0 + s$ and $k_2 = k_0 - s$. The auxiliary functions R_1 , R_2 and R_3 are given by

$$\begin{cases} R_1 = \tilde{x}(u_0 - u_1) + \tilde{y}(v_0 - v_1) + \tilde{z}(w_0 - w_1), \\ R_2 = \tilde{x}(u_0 - u_2) + \tilde{y}(v_0 - v_2) + \tilde{z}(w_0 - w_2), \\ R_3 = p_1 - p_2 + \lambda_2 \rho R_2 - \lambda_1 \rho R_1. \end{cases} \tag{6}$$

- *Hybrid CB scheme.* The conservative form of the equation for total density is used to eliminate the density variable from the momentum equations in (2), which are then solved in conjunction with the advection equations for species transport. The ‘tilde’ variables are given by

$$\begin{cases} \tilde{p} = \frac{1}{s}(\lambda_1 p_2 - \lambda_2 p_1 - \beta(R_1 - R_2)), \\ \tilde{u} = u_0 + \frac{\tilde{x}}{s\rho} R_3, \\ \tilde{v} = v_0 + \frac{\tilde{y}}{s\rho} R_3, \\ \tilde{w} = w_0 + \frac{\tilde{z}}{s\rho} R_3, \\ \tilde{\rho} = \rho_0, \\ \tilde{\rho}_i = \rho_{i0}, \end{cases} \tag{7}$$

where the auxiliary functions R_1 , R_2 and R_3 are defined by (6). In this case, the artificial speed of sound is $s = \sqrt{\lambda_0^2 + 4\frac{\beta}{\rho}}$ and the eigenvalues are k_0 ($N - 1$ eigenvalues), $k_1 = (k_0 + s)/2$ and $k_2 = (k_0 - s)/2$.

- *Conservative CB scheme.* The conservative system (2) is solved without any reductions. The ‘tilde’ variables are given by

$$\begin{cases} \tilde{p} = \frac{1}{s}(\lambda_1 p_2 - \lambda_2 p_1 - \beta(R_1 - R_2)), \\ \tilde{u} = u_0 + \frac{\tilde{x}}{s\rho} R_3, \\ \tilde{v} = v_0 + \frac{\tilde{y}}{s\rho} R_3, \\ \tilde{w} = v_0 + \frac{\tilde{z}}{s\rho} R_3, \\ \tilde{\rho} = \rho_0 + \frac{\rho}{\beta}(p - p_0 + \frac{\lambda_0}{s} R_3), \\ \tilde{\rho}_i = \rho_{i0} + \frac{\rho_i}{\beta}(p - p_0 + \frac{\lambda_0}{s} R_3), \end{cases} \tag{8}$$

where the auxiliary functions R_1 , R_2 and R_3 are defined by (6). In this case, the artificial speed of sound is $s = \sqrt{\lambda_0^2 + 4\frac{\beta}{\rho}}$, $k_1 = (k_0 + s)/2$ and $k_2 = (k_0 - s)/2$.

In all the above cases the ‘tilde’ variables are used to calculate the advective fluxes, where the characteristics variables $\mathbf{V}_l = (p_l, u_l, v_l, w_l, q_l, q_{i,l})^T$ ($l = 0, 1, 2$) are calculated by a Godunov type-scheme

$$\begin{cases} \mathbf{V}_0 = \frac{\mathbf{V}_L + \mathbf{V}_R}{2} - \text{sign}(\lambda_0) \frac{\mathbf{V}_R - \mathbf{V}_L}{2}, \\ \mathbf{V}_1 = \mathbf{V}_L, \\ \mathbf{V}_2 = \mathbf{V}_R, \end{cases} \tag{9}$$

where $\text{sign}(k_0) = 1$ or -1 for $k_0 > 0$ and $k_0 < 0$, respectively. The variables with indices ‘L’ and ‘R’ denote left and right states of intercell values, which are calculated by polynomial interpolation, first-, second- or third-order accurate [3]. Finally, we mention that the solution in pseudo-time is advanced by a fourth-order Runge–Kutta scheme [50] in conjunction with a nonlinear multigrid method that is presented in the next section.

3. Multigrid acceleration

Many of the basic concepts introduced in multigrid methods for elliptic equations [10] are also applicable to the present discussion, but the specific details are different due to the fundamental nature of the equations. In the present case, the multigrid method is applied to solve the coupled system of Eqs. (1). In principle, multigrid can be implemented in conjunction with several grid levels, i.e., five, six or even more, and this is often the case when multigrid is employed to solve elliptic equations such as the pressure-Poisson equation. There are, however, numerical reasons on the basis of which one can argue in favor of a smaller number of grid levels, e.g., 3 grid levels. If the grid on which the equations are to be solved is not fine enough, then the coarsest grid will not encompass a sufficient number of grid points to provide a good correction for the fine grid. Numerical experiments have shown that in the case of (very) coarse grids the multigrid efficiency is significantly reduced. This has been observed in theoretical investigations of multilevel algorithms for non-symmetric (e.g. [51,52]) and nonlinear problems (e.g. [53]). A smaller number of grids also improves the efficiency of parallel computations, as has been demonstrated in previous studies by Ålund et al. [55] and Axelsson and Neytcheva [56,57]. Finally, the use of several grid levels may increase the complexity of the computer code and memory requirements.

For the case of steady flows, the solution of the equations can be obtained by a full multigrid–full approximation storage algorithm (FMG–FAS) on a sequence of coarser grids and this solution can be used as an initial guess for the multigrid procedure. The coarse grid computations provide a good initial guess for the intermediate grid and the same procedure is repeated on the intermediate grid in order to provide a good initial guess for the finest grid. The main steps of the V-cycle implementation of the three-grid algorithm (fine, intermediate and coarse grids) are described below using the following notation (see also Fig. 3): P and R stand for the prolongation and restriction operators; N_{cg} and N_{fg} denote the Navier–Stokes solution on the coarse and fine grids, respectively; 0_{cg} is the initial condition used for the solution; \bar{V} stands for the coarse grid function. The solution algorithm utilized for single grid calculations is also used as a relaxation procedure (S) on the fine (S_{fg}) and intermediate grids (S_{ig}), and as a solver on the coarse grid. The various steps of the three-grid solution are listed below:

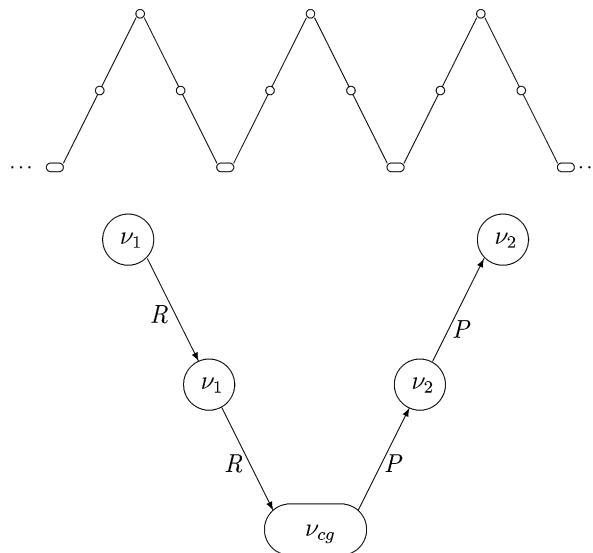


Fig. 3. Schematic of multigrid V-cycle, where m_1 , m_2 and m_{cg} stands for pre-relaxation, post-relaxation and coarse-grid iterations performed on the three grid levels.

- Perform m_1 pre-smoothing iterations on the fine grid, symbolically written as $U_{fg} := S_{fg}(U_{fg}, 0_{fg}, m_1)$.
- Compute finest grid defect, $d_{fg} := N_{fg}U_{fg}$.
- Restriction of the defect to the intermediate grid $d_{ig} := Rd_{fg}$.
- Compute the right-hand side – RHS in (2) – of the Navier–Stokes equations on the intermediate grid, $f_{ig} := -d_{ig} + N_{ig}\bar{V}_{ig}$. The term \bar{V}_{ig} is defined according to Brandt [58] (see discussion below).
- Perform m_1 pre-smoothing iterations on the intermediate grid, $V_{ig} := S_{ig}(V_{ig}, f_{ig}, v_1)$.
- Compute intermediate grid defect, $d_{ig} := -f_{ig} + N_{ig}V_{ig}$.
- Restriction of the defect to the coarse grid, $d_{cg} := Rd_{ig}$.
- Compute the right-hand side of the equations on the coarse grid, $f_{cg} := -d_{cg} + N_{cg}\bar{V}_{cg}$. The term \bar{V}_{cg} is defined according to Brandt [58] (see discussion below).
- Compute coarse grid approximate solution, $V_{cg} := N_{cg}^{-1}f_{cg}$.
- Compute correction on the coarse grid, $c_{cg} := V_{cg} - \bar{V}_{cg}$.
- Prolongation of the correction to the intermediate grid, $c_{ig} := Pc_{cg}$.
- Correct solution on the intermediate grid, $V_{ig} := V_{ig} + c_{ig}$.
- Perform m_2 post-smoothing iterations on the intermediate grid, $V_{ig} := S_{ig}(V_{ig}, f_{ig}, v_2)$.
- Compute correction on the intermediate grid, $c_{ig} := V_{ig} - \bar{V}_{ig}$.
- Prolongation of the correction to the finest grid, $c_{fg} := Pc_{ig}$.
- Correct solution on the finest grid, $U_{fg} := U_{fg} + c_{fg}$.
- Perform m_2 post-smoothing iterations on the finest grid, $U_{fg} := S_{fg}(U_{fg}, 0_{fg}, v_2)$.

The pre-smoothing, post-smoothing and coarsest grid iterations are performed by a fourth-order Runge–Kutta scheme to march the solution in pseudo-time. Note that the Navier–Stokes solver used on the coarse and intermediate grids is slightly different than the original single-grid solver because the RHS of the Navier–Stokes equations becomes zero (upon achieving convergence) only for the single-grid algorithm. In the case of the multigrid method the right-hand side of the equations in the coarse and intermediate grids is not zero due to the additional terms (e.g., $N_{ig}V_{ig}$) arising from the FAS linearization procedure. For unsteady flows the multigrid V-cycles are performed at each time step (Fig. 4). Larger time steps can be used on the coarse and intermediate grids to further reduce the number of iterations on these grid levels.

In the case of linear equations the multigrid solution on the fine grid can be directly computed on coarser grids using the same solution matrix and with the restricted defect being the RHS of the equations. However, this will not lead to efficient solutions in the case of nonlinear problems. In this case the multigrid corrections are formed as differences between some basic reference solution and the currently computed

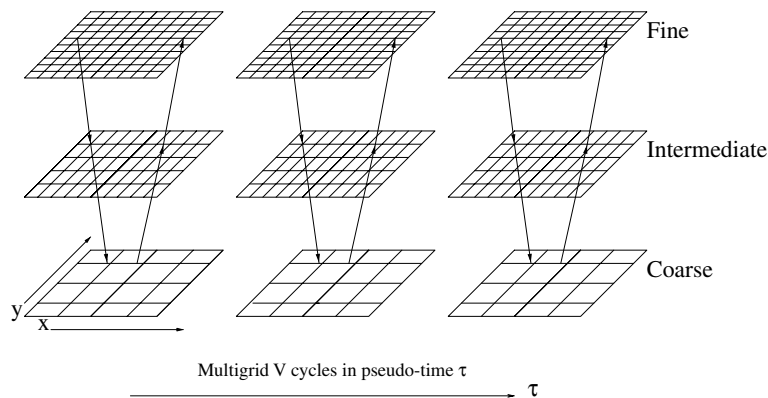


Fig. 4. Schematic of multigrid implementations for time-dependent problems. Multigrid V-cycles are performed at each real time step in order to achieve convergence in pseudo-time τ .

approximation of this solution. Therefore, the three-grid FAS algorithm requires the calculation of the so-called *coarse-grid* functions. In the case of the three-grid algorithm these functions need to be defined for the coarse, \bar{V}_{cg} , and intermediate grids, \bar{V}_{ig} , respectively. Here, we follow the strategy suggested by Brandt [58] that is to calculate these functions as projections of the current intermediate and finest grid solutions onto the coarse and intermediate grids, respectively: $\bar{V}_{cg} = RV_{ig}$, $\bar{V}_{ig} = RU_{fg}$, where R is the restriction operator.

The efficiency of the multigrid solution depends on the relaxation steps at different grid levels, i.e., pre- (m_1) and post-relaxation (m_2) iterations, as well as iterations on the coarse grid (m_{cg}). We have performed several numerical experiments, which have shown that for the ‘unsteady-type’ multigrid employed here, the equations do not have to fully converge on the coarsest grid for achieving the best multigrid efficiency. Moreover, numerical experiments have indicated that although the number of pre- and post-relaxation iterations depends on the flow case, 6–12 iterations are sufficient. In order to comparatively examine the efficiency of different CB schemes in variable-density flow computations, we have used fixed multigrid cycle parameters for all test cases, comprising of 10 pre-smoothing and post-relaxation iterations on the fine grid; no pre-smoothing and 10 post-relaxation iterations on the intermediate grids; and 1500 iterations on the coarsest grid; computations on each grid level are performed until either the maximum number of iterations is reached or the solution is converged.

The implementation of multigrid requires restriction and prolongation operators to be defined. The restriction operator can be simply defined by considering that any coarse-grid control volume (CV) consists of eight fine grid CVs (in three dimensions). In simple geometries, this can be achieved by covering the computational domain with a coarse grid and further refine it in such a way that any coarse-grid volume is split into eight fine-grid volumes. For complex geometries it is better to first generate the finest grid, and then construct the coarser grids by eliminating lines of the fine grid. Then, the restriction operator is defined by the weighted summation of all the values over the fine-grid CVs.

Multigrid algorithms can be implemented using different prolongation operators. The simplest definition of the prolongation operator is the linear interpolation (Fig. 5). If U^f and U^c are the values of the variable U on the fine and coarse grids, respectively, and assuming that in one dimension the fine-grid cells with indices $(2i - 1)$ and $(2i)$ will form a coarse-grid cell (i) , then the fine-grid values are obtained by the coarse-grid ones as follows:

$$U_{2i}^f = \frac{1}{4}U_{i+1}^c + \frac{3}{4}U_i^c, \quad U_{2i+1}^f = \frac{3}{4}U_{i+1}^c + \frac{1}{4}U_i^c. \tag{10}$$

For two- and three-dimensional cases, bilinear or trilinear prolongation formulas can be obtained by combining one-dimensional linear interpolation. If $(2i, 2j, 2k)$ are the indices of the fine-grid cell in three dimensions, the trilinear prolongation operator is then defined by

$$U_{2i,2j,2k}^f = \frac{1}{64}U_{i+1,j+1,k+1}^c + \frac{3}{64}U_{i+1,j+1,k}^c + \frac{3}{64}U_{i+1,j,k+1}^c + \frac{3}{64}U_{i,j+1,k+1}^c + \frac{9}{64}U_{i+1,j,k}^c + \frac{9}{64}U_{i,j+1,k}^c + \frac{9}{64}U_{i,j,k+1}^c + \frac{27}{64}U_{i,j,k}^c. \tag{11}$$

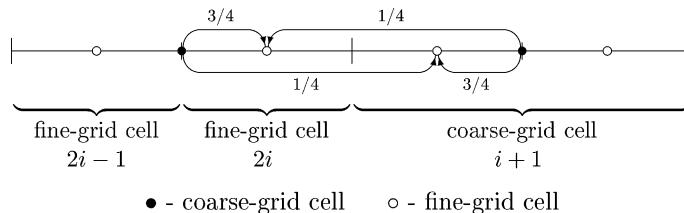


Fig. 5. Schematic of the one-dimensional linear interpolation.

4. Diffusion broadening studies

The diffusion broadening problem (Fig. 1) provides a test bed for investigating the accuracy and efficiency of the numerical methods discussed here. The flow setup comprises of two miscible fluids of different densities entering a channel of rectangular cross section through two rectangular inlets and flowing in a microfluidic slit. Ismagilov et al. [30] derived analytic solutions for the dependence of the diffusion front position on the distance from the inlets and found that the position of the diffusion front is proportional to $x^{\frac{1}{2}}$ in the middle of the channel and to $x^{\frac{1}{3}}$ near the wall. These results were found to be in good agreement with experiments [30,31], approximate models [32,33] and solutions of the diffusion equations based on ‘frozen’ flow conditions [31], i.e., solving only the advection–diffusion equations for species transport for a prescribed flow field. In our numerical investigation we have considered both 2-D and 3-D flows at low Reynolds numbers typical for microfluidic applications, $Re \in [25, 100]$, and for a fixed value of Peclet number $Pe = 10^3$. Density variations are typically small in diffusion broadening problems, where usually both streams contain a dilute solution of diffusing species. In the present study and in order to assess the ability of the numerical schemes to accurately capture the contact discontinuity, the dimensionless densities of the two fluids were chosen to be 1.0 and 0.8, respectively. Moreover, we considered both fluids having the same viscosity in order to reduce the number of parameters involved in the investigation. The velocity boundary condition at the inlets is given by a parabolic profile normalized by the maximum inlet velocity. At the outlet the velocities are obtained by extrapolation considering that the channel is long enough to allow fully developed flow to be established. The pressure is considered constant and equal to 1 (dimensionless) at the outlet, while it is obtained by linear extrapolation in the boundary cells at the inlet. The densities of the fluids are constant at the inlets, with each inlet occupied by one fluid. As an initial condition, we have employed parabolic velocity profiles and constant pressure equal to 1 everywhere. Initially, the heavier fluid occupies one inlet and the channel downstream, while the second inlet is occupied by the lighter fluid. For the present problem and Reynolds number, the no-slip boundary condition on the wall is still valid. The computational grid has been clustered near the entrance of the main section. In the 2-D computations, the fine grid contained 37×37 and 197×73 grid points in the inlets and main sections, respectively. In the 3-D computations, the fine grid contained $17 \times 17 \times 17$ and $57 \times 33 \times 17$ grid points in the inlets and main sections, respectively. Fig. 6(a) shows the grid used in the 2-D computations near the entrance to the main section; the coordinates were non-dimensionalized using the inlet height as a characteristic length. The CFL numbers used for defining the time steps (the pseudo-time step depends on the CFL number for stability reasons) for the 2-D and 3-D computations were 0.2 and 0.1, respectively. Computations have been carried out both for 2-D and 3-D cases with channel lengths 27 and 40 inlet heights for the 3-D and 2-D cases, respectively, and inlet length of one inlet height in both cases. The development of the flow field for the 2-D case in the entrance section is shown in Fig. 6(b) by means of u -velocity contours. The results in this figure have been obtained for $Re = 50$ using the conservative CB scheme with third-order polynomial interpolation.² The slight asymmetry of the streamlines in Fig. 6(b) is due to the fact that the flow is not yet fully developed. For the 2-D case, an exact analytic solution is available for the velocity of the fully developed flow in the main section of the channel [42]; this is a parabolic profile since the fluids hold the same viscosities. The development of the velocity profile as computed using the conservative CB scheme is shown in Fig. 7(a), while Fig. 7(b) shows the comparison between analytic and computed solutions. Analytic estimates [30] indicate that the diffusion profile for a 2-D case is governed by a power law with exponent 0.5. In our investigation, for a 2-D case we have defined the diffusion front position as the point where species density falls below 20% of its density at the inlet (the position of diffusion front inside a grid cell was obtained by linear interpolation). Fig. 8 shows the development of diffusion fronts, in logarithmic scale, as

² The Reynolds number calculation is based on the maximum inlet velocity, viscosity of the fluids at the inlet and inlet height.

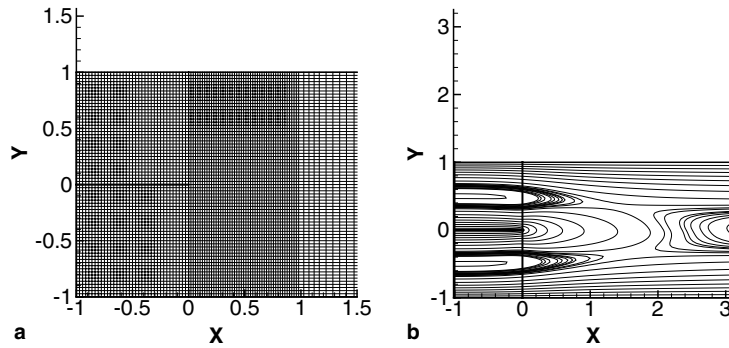


Fig. 6. Enlargement of the computational mesh (left plot) and u -velocity contours in the entrance region of the main channel (right plot) at $Re = 50$: (a) mesh; (b) u -velocity contours.

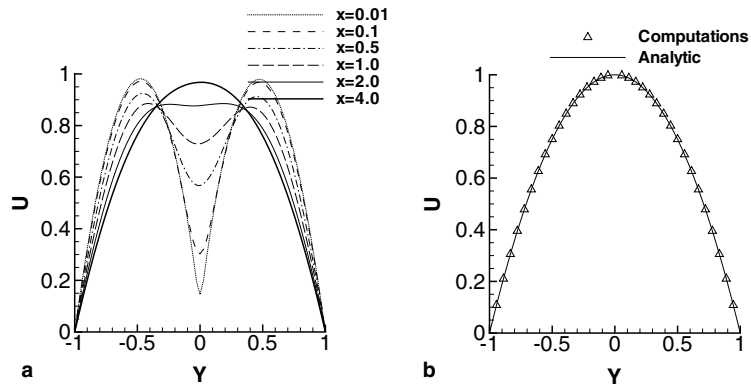


Fig. 7. Velocity profile development for the 2-D case at $Re = 50$ and comparison between the analytic and numerical solution for the fully developed flow profile: (a) velocity profile development; (b) outlet velocity.

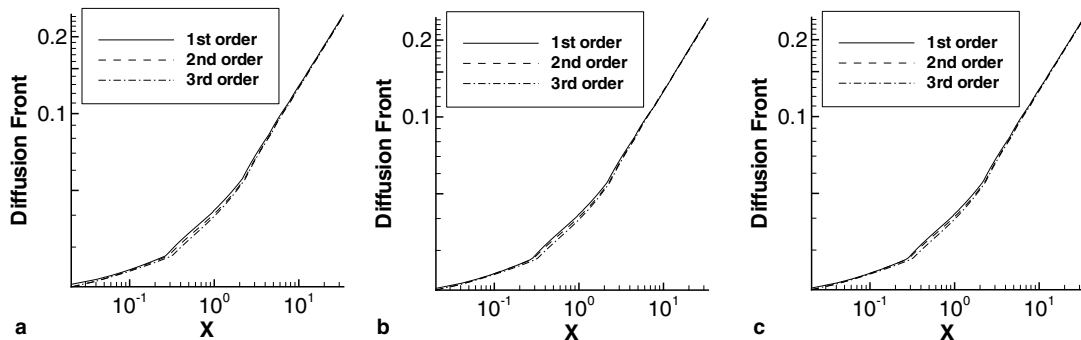


Fig. 8. Results for 2-D diffusion fronts ($Re = 50$) using different CB schemes and order of intercell interpolation: (a) conservative CB scheme; (b) hybrid CB scheme; (c) transport CB scheme.

Table 1
Accuracy of 2-D diffusion broadening slopes computations on the basis of percentage differences from the analytic solution

Numerical scheme	Interpolation order		
	1st order (%)	2nd order (%)	3rd order (%)
Conservative CB scheme	3.10	1.28	0.46
Hybrid CB scheme	3.22	1.30	0.46
Transport CB scheme	3.06	1.30	0.46

obtained by different CB schemes (transport, conservative and hybrid) and different orders of polynomial interpolation. As expected, the results show that the power-law dependency is established only in the region along the channel where the velocity profile is fully developed. For the 2-D case (Fig. 8), a deviation of 5% for the u -velocity value at the center line of the main channel from its value when the flow becomes fully developed flow, was reached at the distance of 3.5 inlet heights. The deviations of the computationally obtained slopes from the analytic value of 0.5 are summarized in Table 1. The accuracy of the solution increases with the order of interpolation. The discrepancies between different CB schemes are below 0.16% and further decrease as we increase the order of polynomial interpolation.

Fig. 9 shows cross section density profiles in the main channel. These profiles provide information about how accurately the contact discontinuity has been resolved. The best results were obtained by third-order interpolation. The resolution of discontinuity exhibited no significant dependence on the variables reconstruction method, with the results varying slightly for the first-order interpolation but becoming identical for all CB schemes when using third-order interpolation. All the CB schemes investigated here are nominally second-order accurate. Nevertheless, the accuracy of the computational results depends on the polynomial interpolation as shown by the calculation of the diffusion slopes in Table 1. To numerically examine the order of accuracy obtained by different polynomial interpolations, we have carried out grid convergence studies using three uniform grids containing 28×24 , 56×48 and 112×96 computational cells in the main channel section, respectively. We have used the average of the absolute value of the u -velocity throughout the computational domain, u_{av} , in order to analyze the grid convergence for all the CB schemes and orders of polynomial interpolation. The grid convergence, n_{gr} , can be estimated as

$$n_{gr} = \frac{\ln |(u_{av}^{coarse} - u_{av}^{medium}) / (u_{av}^{fine} - u_{av}^{medium})|}{\ln 2}, \tag{12}$$

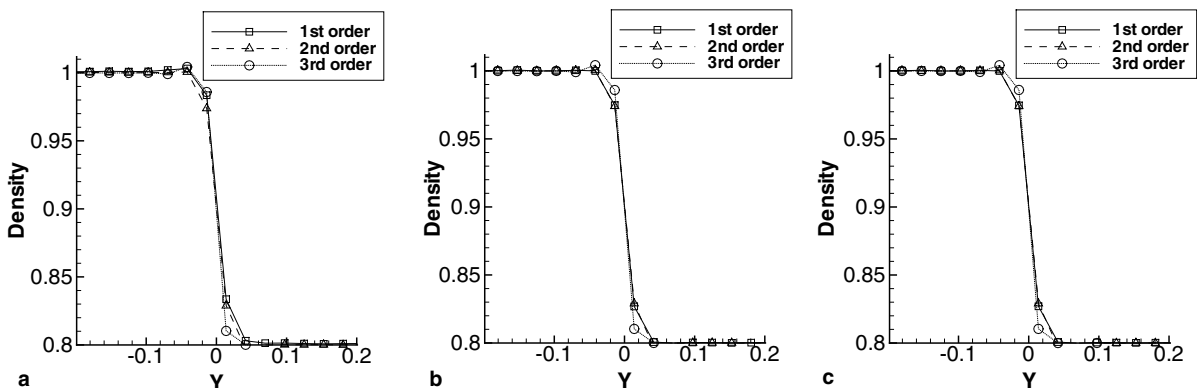


Fig. 9. Density profiles ($x = 17$) as predicted by different CB schemes and orders of interpolation: (a) conservative CB scheme; (b) hybrid CB scheme; (c) transport CB scheme.

Table 2

Number of multigrid cycles required to reach convergence for 2-D diffusion broadening computations at $Re = 50$

	1st order	2nd order	3rd order
Transport CB scheme	33	44	171
Hybrid CB scheme	26 (–21%)	36 (–18%)	134 (–22%)
Conservative CB scheme	24 (–27%)	32 (–27%)	115 (–33%)

The values in brackets give the percentage reduction in the number of multigrid cycles compared to the transport CB scheme (slowest convergence).

Table 3

Predicted orders of accuracy for different CB schemes and variables interpolation in relation to the diffusion broadening computations

	1st order	2nd order	3rd order
Transport CB scheme	1.71	1.99	1.98
Hybrid CB scheme	1.67	1.96	1.93
Conservative CB scheme	1.67	1.95	1.92

where u_{av}^{coarse} , u_{av}^{medium} and u_{av}^{fine} are the average velocity values obtained on the coarse, medium and fine grids, respectively. The results of Table 3 show that second-order of accuracy (approximately) is obtained by the transport, hybrid and conservative CB reconstructions, where the small discrepancies between second and third-order polynomial interpolations are within the error margin of the convergence rate estimation.

To examine the convergence behavior of different schemes variants we have used as convergence criterion the maximum of the solution variation within a pseudo-time step (complete Runge–Kutta cycle) normalized by the maximum variation obtained in the first step of the pseudo-time iteration; this criterion is henceforth labeled as Runge–Kutta residual. The solution was considered to be converged when the initial Runge–Kutta residual had been reduced by three-order of magnitudes, which corresponds to actual magnitude of solution difference of the order 10^{-5} – 10^{-6} .

Fig. 10 shows the Runge–Kutta residual norms for 2-D computations at $Re = 50$ for the three variants of the CB schemes using first-order (Fig. 10(a)), second-order (Fig. 10(b)) and third-order polynomial interpolations (Fig. 10(c)). The conservative CB scheme consistently exhibits faster convergence rates. The actual number of multigrid cycles required to reach convergence is summarized in Table 2, where the values in

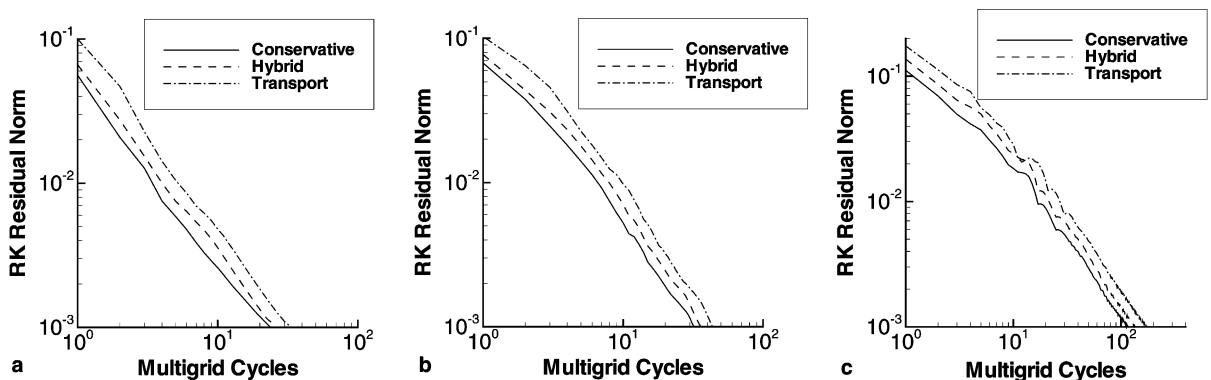


Fig. 10. Multigrid convergence for 2-D diffusion broadening computations using different CB schemes and orders of variables interpolation: (a) first-order interpolation; (b) second-order interpolation; (c) third-order interpolation.

brackets give the percentage reduction in the number of multigrid cycles compared to the transport CB scheme (slowest convergence).

In addition to the 2-D numerical studies, 3-D computations were also performed. The diffusion front and u -velocity development for the 3-D case are shown in Fig. 11. The diffusion front position was defined as the point where species density falls below 20% of its density at the inlet. Fig. 12 shows the position of the diffusion front (in log scale) calculated on the channel’s wall and centerline at $Re = 50$, for the three CB schemes, conservative (Fig. 12(a)), hybrid (Fig. 12(b)) and transport schemes (Fig. 12(c)). The experimental diffusion front slopes correspond to the ones obtained in [30,31]. The results shown in Fig. 12 were obtained using third-order polynomial interpolation. Note that the power-law dependency as obtained by analytic estimations [30] is not applicable in the entrance region, where the flow is not yet fully developed.

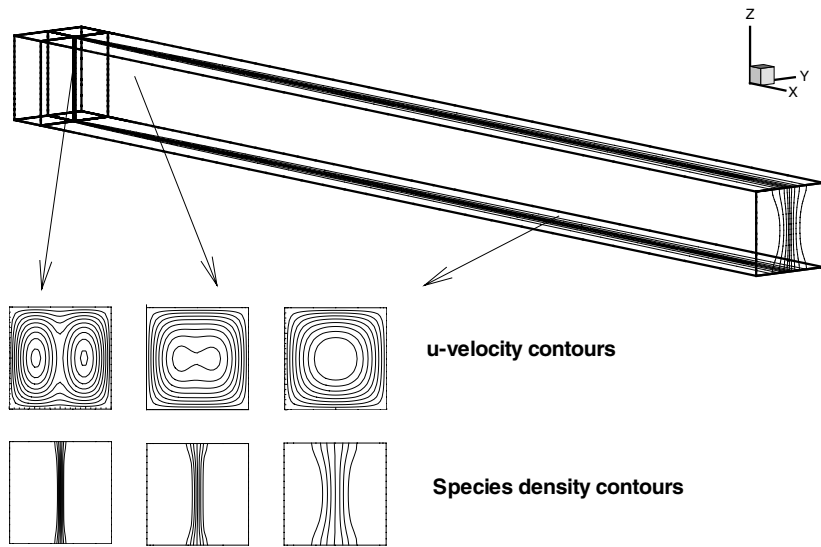


Fig. 11. Development of the diffusion front in 3-D computations.

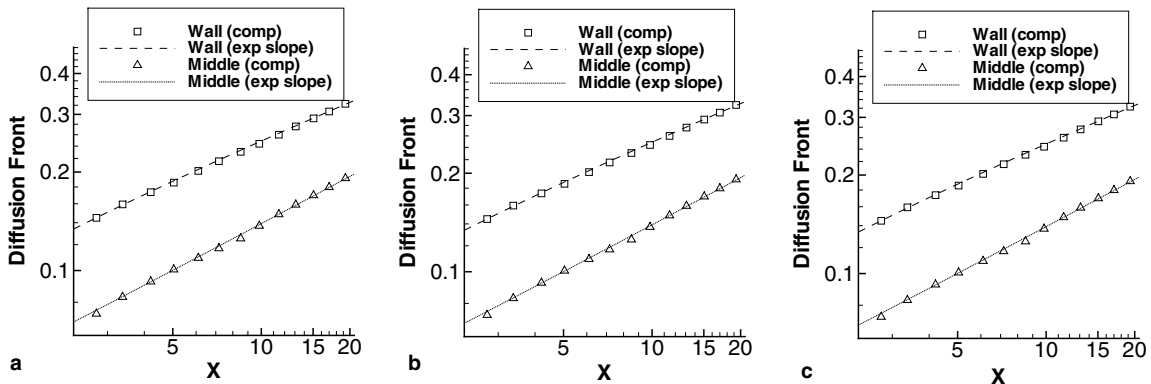


Fig. 12. Comparison of diffusion front predictions with experimental data [30,31] (3-D case, $Re = 50$): (a) conservative CB scheme; (b) hybrid CB scheme; (c) transport CB scheme.

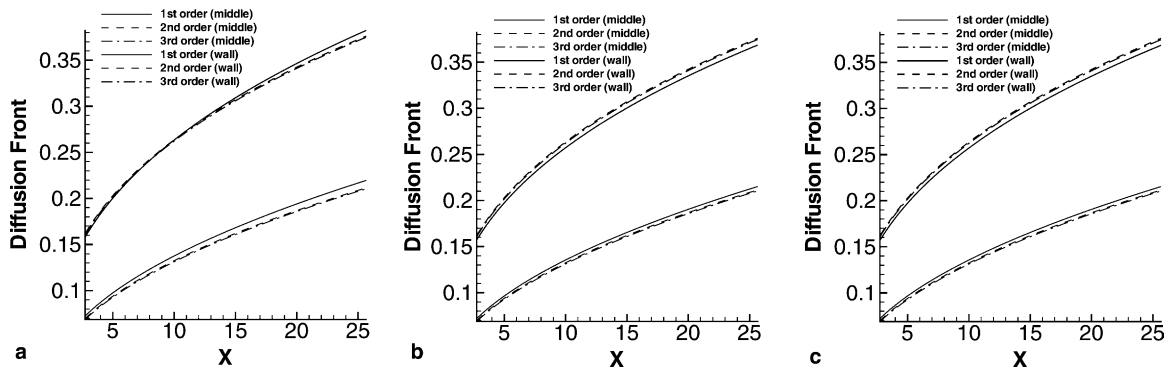


Fig. 13. Diffusion front development (3-D case, $Re = 50$) as predicted by different CB schemes and orders of variable interpolation: (a) conservative CB scheme; (b) hybrid CB scheme; (c) transport CB scheme.

Fig. 13 shows the dependency of the diffusion fronts on the order of polynomial interpolation for conservative (Fig. 13(a)), hybrid (Fig. 13(b)) and transport schemes (Fig. 13(c)) of CB schemes. The deviation of the calculated slopes from the experimental values in the channel's centerline and on the channel's wall are summarized in Tables 4 and 5, respectively. The conservative scheme in conjunction with second/third order interpolations provides overall the best results. This is shown with respect to the calculation in the channel's centerline. The results on the wall exhibit a slightly different tendency with the transport and hybrid CB schemes, first-order interpolation based, to provide the best accuracy; noting, however, that the discrepancies of the conservative, CB scheme against the experimental results is also very small.

The efficiency of the computations in terms of multigrid convergence was found to be dependent on the CB scheme employed. Fig. 14 shows the Runge–Kutta residual norms for all CB schemes (3-D computations at $Re = 50$) for first (Fig. 14(a)), second (Fig. 14 b) and third-order polynomial interpolation (Fig. 14(c)), respectively, in logarithmic scale. The conservative CB scheme provided the best (fastest) multigrid convergence regardless of the polynomial interpolation used. The transport CB scheme resulted in the

Table 4

Accuracy of 3-D diffusion broadening slopes computations in the channel's centerline on the basis of percentage differences from the experimental data

Numerical scheme	Interpolation order		
	1st order (%)	2nd order (%)	3rd order (%)
Conservative CB scheme	1.73	1.26	1.13
Hybrid CB scheme	1.42	1.30	1.17
Transport CB scheme	1.45	1.30	1.18

Table 5

Accuracy of 3-D diffusion broadening slopes computations on the channel's wall on the basis of percentage differences from the experimental data

Numerical scheme	Interpolation order		
	1st order (%)	2nd order (%)	3rd order (%)
Conservative CB scheme	0.90	0.73	0.78
Hybrid CB scheme	0.66	0.79	0.73
Transport CB scheme	0.66	0.77	0.78

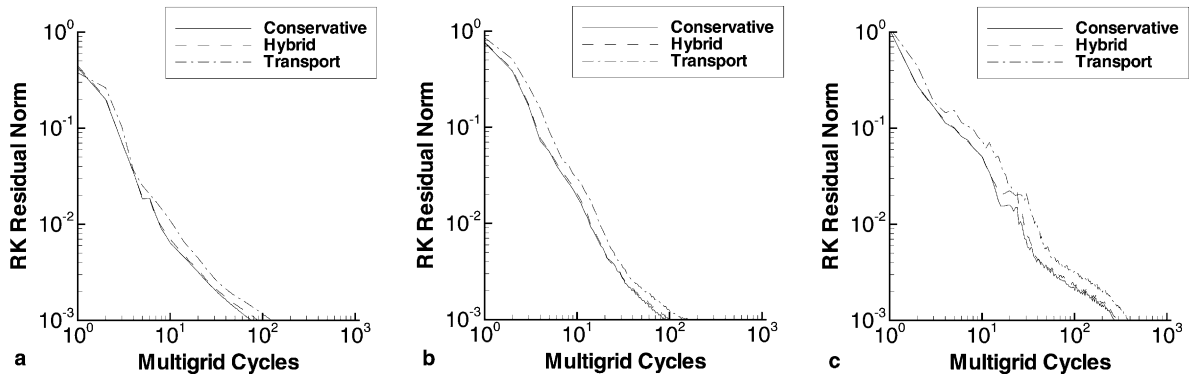


Fig. 14. Multigrid convergence for different CB schemes (3-D diffusion broadening case, $Re = 50$): (a) first-order interpolation; (b) second-order interpolation; (c) third-order interpolation.

slowest convergence. The number of multigrid cycles required to reach convergence is also summarized in Table 6, where the values in brackets give the percentage reduction of the number of multigrid cycles compared to the transport CB scheme (slowest case).

Finally, numerical tests were performed to examine the convergence behavior at different Reynolds numbers. In Fig. 15 results are presented for different Reynolds numbers and orders of polynomial interpolation in conjunction with the conservative CB scheme. Further, in Table 7 the convergence results, in terms of total multigrid cycles, are given for the three CB schemes. The results show that: (i) the numerical convergence is improved at higher Reynolds numbers for all CB schemes; and (ii) the conservative CB scheme yields better convergence for all Reynolds numbers (see Table 7).

5. Variable-density mixing layer

Computations have also been performed for a 2-D, inviscid, variable-density, temporally developed, mixing layer in order to gain insight into the dissipative properties of the characteristics-based schemes as well as multigrid efficiency in combination with different polynomial interpolations. The setup of the problem comprises of a variable-density mixing layer defined by hyperbolic tangent velocity and density profiles (Fig. 2)

$$\begin{cases} \rho = 2 + \tanh(y), \\ u = \tanh(y), \end{cases} \tag{13}$$

where the density ratio between the streams $q_0/q_1 = 3$. Sinusoidal wave perturbations are imposed to the profiles. The wave number, a , of the perturbations corresponds to the most unstable mode for a single-fluid mixing layer with the same velocity profile, i.e., $a = 0.4446$ and wavelength $k \approx 14.13$ [36]. The amplitude of the perturbations is taken to be 1% of the wavelength. For the purpose of the numerical experiments the

Table 6
Number of multigrid cycles required to reach convergence for 3-D diffusion broadening computations at $Re = 50$

	1st order	2nd order	3rd order
Transport CB scheme	124	141	378
Hybrid CB scheme	90 (-27%)	102 (-28%)	301 (-20%)
Conservative CB scheme	76 (-39%)	89 (-37%)	275 (-27%)

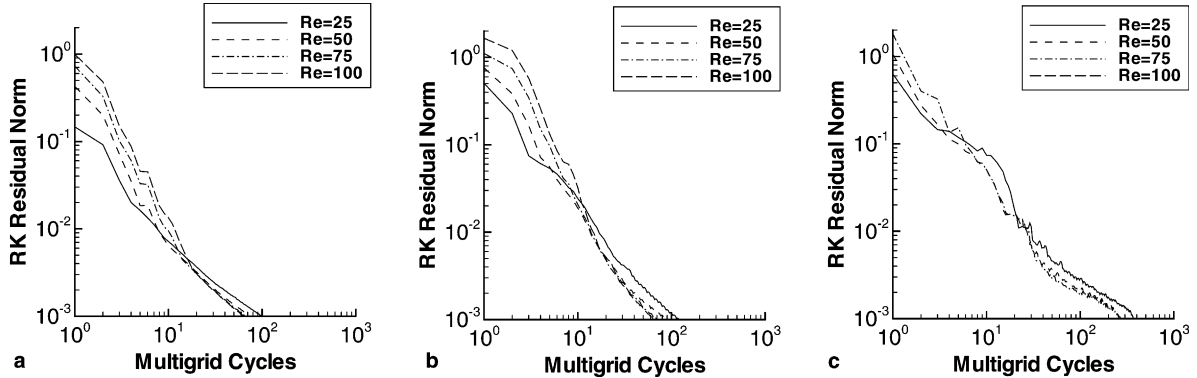


Fig. 15. Dependence of multigrid convergence on the Reynolds number for the diffusion broadening problem: (a) first-order interpolation; (b) second-order interpolation; (c) third-order interpolation.

Table 7

Number of multigrid cycles required to reach convergence for 3-D diffusion broadening computations at different Reynolds numbers

	$Re = 25$	$Re = 50$	$Re = 75$	$Re = 100$
Transport CB scheme	144	124	104	92
Hybrid CB scheme	108 (-25%)	90 (-27%)	75 (-28%)	71 (-23%)
Conservative CB scheme	99 (-31%)	76 (-39%)	67 (-36%)	63 (-32%)

problem is considered to be inviscid and, therefore, diffusion cannot occur because both diffusion and viscosity have the same molecular origin. In the absence of viscosity, diffusion can occur in the case of a dilute solution or particles diffusion (see, e.g. [54]).

The dimensions of the computational domain correspond to two wavelengths of the initial perturbation, i.e., $\{(x, y): x \in [0, 2k], y \in [-k, k]\}$. The computational grid consists of 117×117 grid points. We have used periodic boundary conditions on the left and right boundaries and no-slip boundary conditions on the upper and lower boundaries in the y direction. All unsteady computations were performed with $CFL_p = 0.07$ in pseudo-time and $CFL_r = 0.2$ in real time, where for the present problem the pseudo-time and real time steps are defined by $D\tau_{i,j,k} = CFL_p / (\max_{m=1-6}\{|k_1|, |k_2|\})_{i,j,k}$ and $Dt_{i,j,k} = CFL_r / (\max_{m=1-6}\{|k_1|, |k_2|\})_{i,j,k}$, respectively, where m stands for the six faces of the computational cell in 3-D.

The evolution of the mixing layer is illustrated in Fig. 16 by means of the density contours at different time instants. These results have been obtained by the conservative CB scheme and third-order polynomial interpolation. The results show that the center of the vortex is displaced towards the lighter fluid as also predicted in previous studies [44,46,47]. Fig. 17 shows the density contours at dimensionless time $t = 25$ as obtained by using the conservative CB scheme in conjunction with first-, second- and third-order interpolation. The least dissipative solution is obtained by third-order interpolation, while the first-order interpolation gives very dissipative results. The discrepancies between second and third-order are not significant on the 117×117 grid (Fig. 16), but become greater as the grid is further coarsened. Fig. 18 illustrates development of the density layer on a coarser grid (57×57), as obtained by the conservative CB scheme and third-order polynomial interpolation. Fig. 19 compares the density contours at dimensionless time $t = 25$ using the conservative CB scheme in conjunction with first-, second- and third-order interpolation on the coarse grid. It can be seen that the third-order interpolation significantly reduces numerical dissipation. Fig. 20 shows the development of the mixing layer thickness in time as obtained by different CB schemes in conjunction with different orders of interpolation. The results exhibit slight differences when the CB

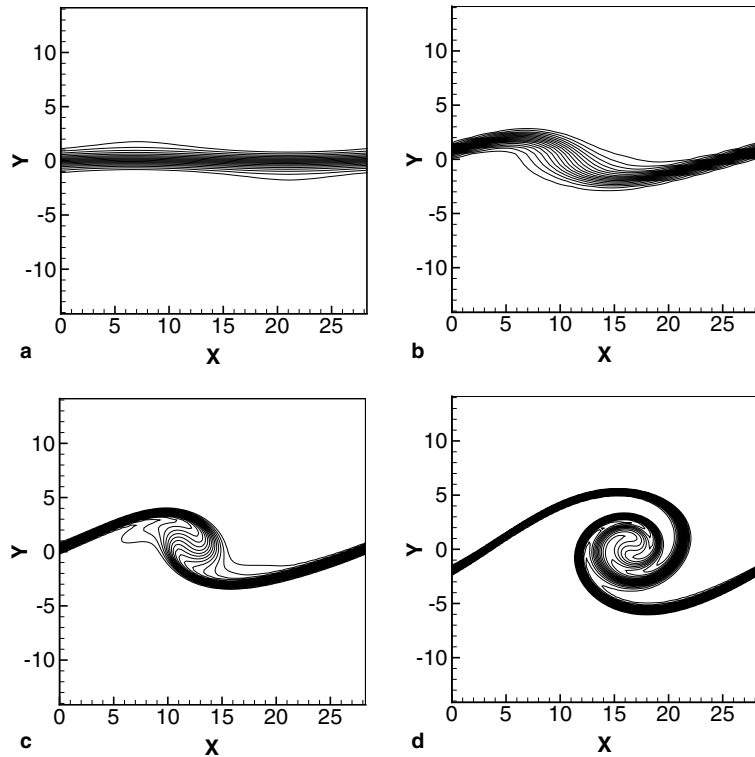


Fig. 16. Development of the mixing layer flow at different time instants as obtained by the conservative CB scheme with third-order interpolation: (a) $t = 0$; (b) $t = 10$; (c) $t = 15$; (d) $t = 25$.

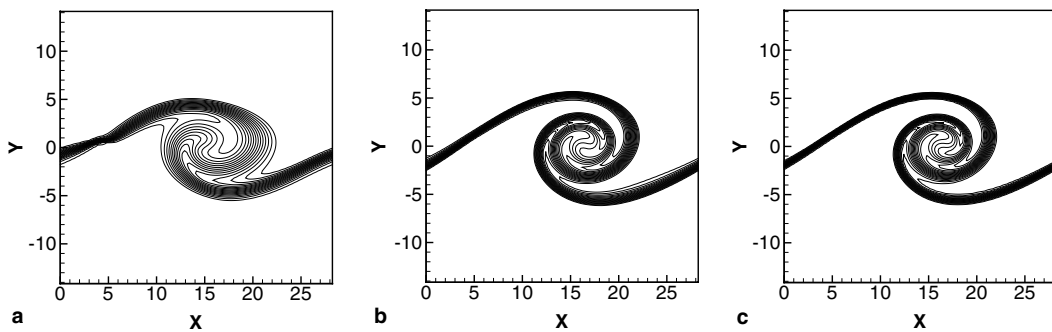


Fig. 17. Numerical solution at $t = 25$ (dimensionless) as predicted by the conservative CB scheme using different orders of variable interpolation: (a) first-order interpolation; (b) second-order interpolation; (c) third-order interpolation.

schemes are used with first-order interpolation but overall the choice of the CB scheme has negligible effects on the results. Furthermore, Fig. 21 shows the mixing layer thickness dependency on the order of polynomial interpolation for conservative, hybrid and transport schemes. Both second- and third-order variants exhibit very similar results.

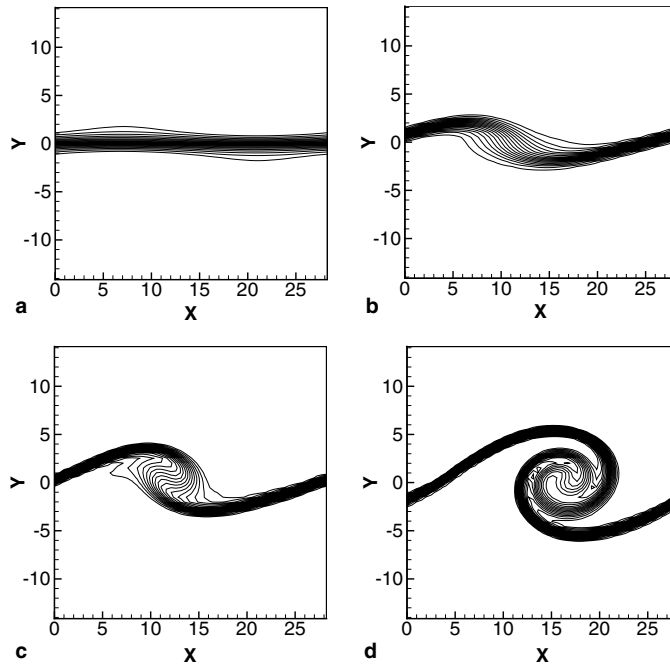


Fig. 18. Development of the mixing layer flow at different time instants as obtained by the conservative CB scheme with third-order interpolation (57×57 grid): (a) $t = 0$; (b) $t = 10$; (c) $t = 15$; (d) $t = 25$.

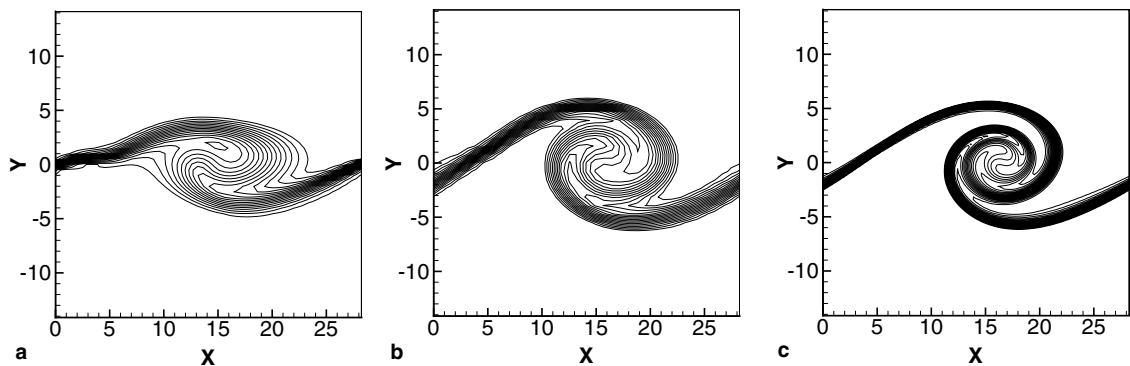


Fig. 19. Numerical solution on the coarse grid (57×57) at $t = 25$ (dimensionless) as predicted by the conservative CB scheme using different orders of variable interpolation: (a) first-order interpolation; (b) second-order interpolation; (c) third-order interpolation.

The convergence performance was investigated for different CB schemes and interpolation variants. For unsteady flows, the norm of the variables derivatives in pseudo-time was employed as parameter to monitor convergence at each time step. The solution was considered to converge when the maximum of all norms reached 10^{-4} . For the artificial-compressibility-based methods considered in this study, we have observed that the maximum number of multigrid cycles required to reach convergence occurs in the first time step. This is due to the nature of the artificial-compressibility formulation, which cannot satisfy the divergence-free constraint per se, but instead requires this to be iteratively obtained. Therefore, we have used two criteria to compare multigrid convergence of different schemes: the first one is the number of multigrid cycles required to reach convergence at the first time step and the second one is the total number of multigrid

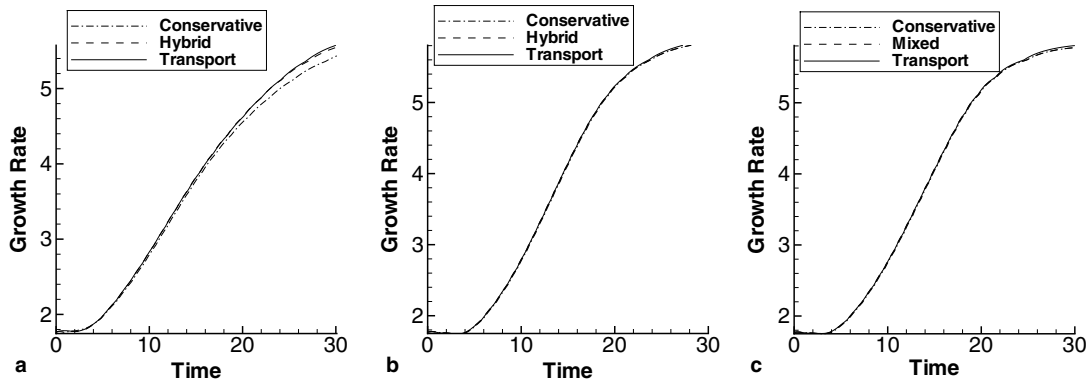


Fig. 20. Dependence of mixing layer thickness on the CB scheme employed in the computations: (a) first-order interpolation; (b) second-order interpolation; (c) third-order interpolation.

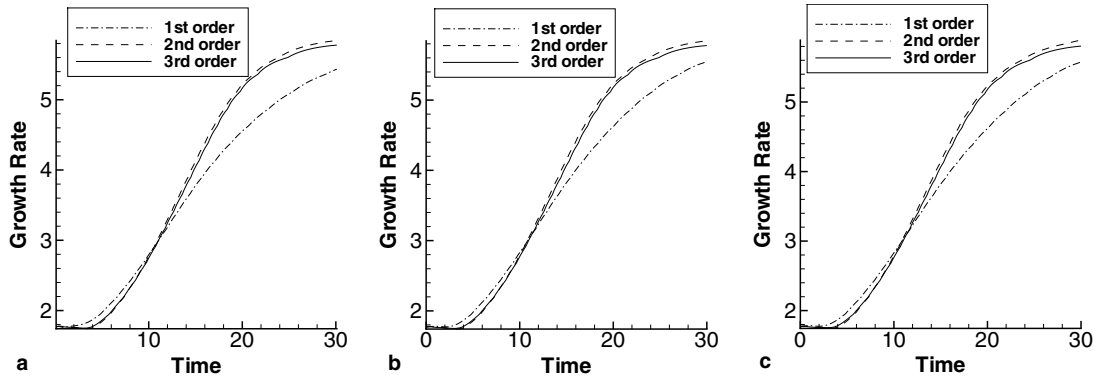


Fig. 21. Mixing layer thickness dependence on the order of variables interpolation. The difference between the second- and third-order interpolation appearing for $t > 15$ remain less than 2.5% even at late times, $t > 25$: (a) conservative CB scheme; (b) hybrid CB scheme; (c) transport CB scheme.

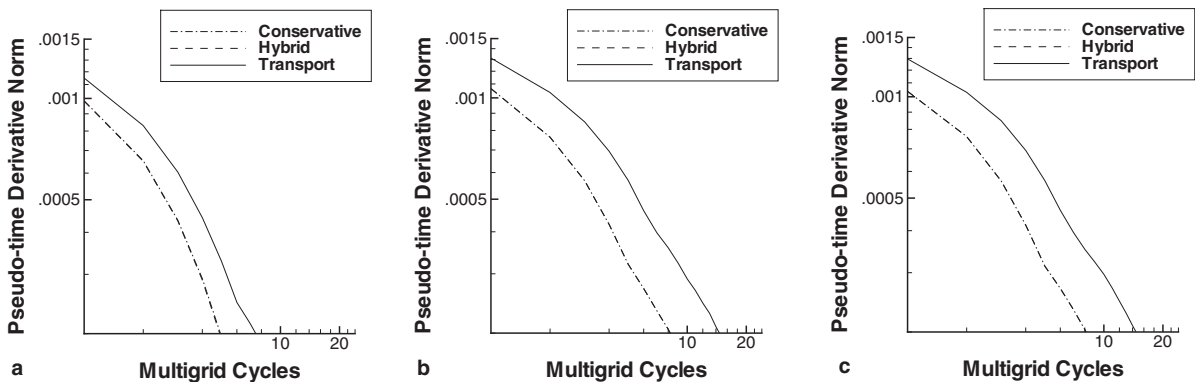


Fig. 22. Multigrid convergence for the mixing layer flow using different CB schemes and orders of variables interpolation: (a) first-order interpolation; (b) second-order interpolation; (c) third-order interpolation.

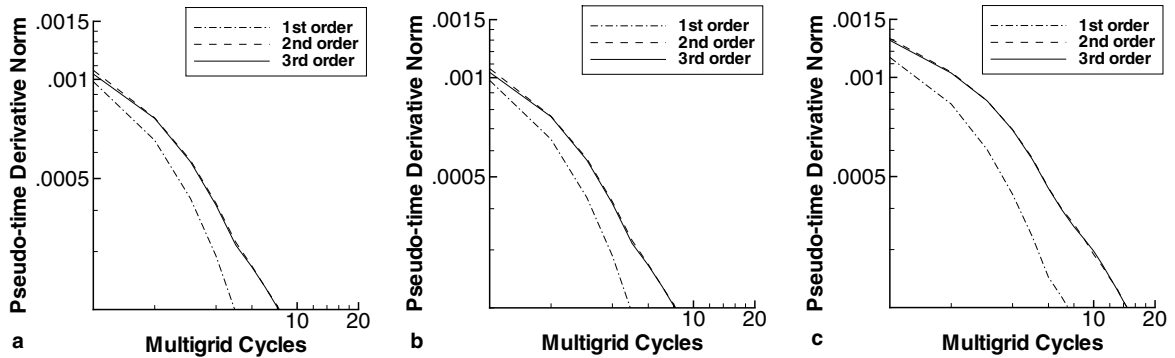


Fig. 23. Multigrid convergence dependence on the order of variables interpolation, for the mixing layer flow: (a) conservative CB scheme; (b) hybrid CB scheme; (c) transport CB scheme.

Table 8

Number of multigrid cycles required to reach convergence at the first time step for the mixing layer problem

	1st order	2nd order	3rd order
Transport CB scheme (fine grid)	14	25	25
Hybrid CB scheme (fine grid)	8	15	15
Conservative CB scheme (fine grid)	8	15	15
Transport CB scheme (coarse grid)	12	33	25
Hybrid CB scheme (coarse grid)	10	25	18
Conservative CB scheme (coarse grid)	10	25	18

Table 9

Number of multigrid cycles required for $t = 30$ (dimensionless)

	1st order	2nd order	3rd order
Transport CB scheme (fine grid)	580	1762	1748
Hybrid CB scheme (fine grid)	431 (–26%)	1289 (–27%)	1156 (–34%)
Conservative CB scheme (fine grid)	375 (–35%)	1267 (–28%)	1150 (–34%)
Transport CB scheme (coarse grid)	644	4687	3620
Hybrid CB scheme (coarse grid)	580 (–10%)	3801 (–19%)	2268 (–37%)
Conservative CB scheme (coarse grid)	534 (–17%)	3672 (–22%)	2254 (–38%)

cycles throughout the computation up to a prescribed time instant ($t = 30$, dimensionless, in the present numerical experiments). Figs. 22 and 23 show the reduction of the residual norm in pseudo-time (first real time step) for the three CB variants in conjunction with first-, second- and third-order interpolation schemes. The hybrid and conservative schemes exhibit the same convergence, whereas the transport variant results in slower convergence. The number of multigrid cycles required to reach convergence at the first time step is listed in Table 8 both for coarse and fine grid computations. Interestingly, second and third-order interpolation schemes require the same number of multigrid cycles on the fine grid. However, if we consider the multigrid cycles for the entire computation (see Table 9, results corresponding to $t = 30$), it is seen that the third-order interpolation results in faster convergence speed compared to second-order. In Table 9, the values in brackets give the percentage reduction of the number of multigrid cycles compared to the transport scheme (slowest method). As expected, the difference between second and third-order interpolation schemes in terms of multigrid cycles is reduced when refining the grid. Overall, the results reveal that similar to the diffusion broadening studies the conservative CB scheme provides the best multigrid convergence.

6. Conclusions

A numerical study for the accuracy and efficiency of artificial-compressibility CB schemes for variable-density incompressible flows, was presented. The study involved three different CB schemes in conjunction with three intercell interpolation variants and multigrid acceleration. The differences in the design of the CB schemes arise from the origin of the variable-density formulation of the governing system of equations. Both steady and unsteady flow problems were employed to assess the accuracy and efficiency of the schemes. The steady flows cases concerned 2-D and 3-D diffusion broadening flows through microfluidics and the unsteady flow concerned the temporal development of a variable-density mixing layer.

The results for all CB schemes were found to be in good agreement with analytical and experimental data with better results being obtained when using the CB schemes in conjunction with second and third-order intercell interpolation. It was, however, shown that multigrid convergence depends on the CB variant as well as on the polynomial interpolation used at the cell faces of the computational volume.

The (viscous) flow computations through microfluidics showed that the conservative CB scheme exhibits better multigrid convergence compared to the hybrid and transport schemes, e.g., for 3-D computations the conservative CB scheme resulted in up to 39% reduction in multigrid cycles compared to the transport CB scheme. This can be explained by the fact that the conservative formulation has a direct effect on the speed of density disturbances during the pseudo-time iterations. The computations also revealed that the difference, in terms of multigrid cycles required to achieve convergence, between hybrid and conservative schemes is smaller compared to that between hybrid and transport schemes. Both in transport and hybrid schemes, the densities are reconstructed along streamlines and, essentially, the only difference between these two formulations is the absence of the velocity divergence condition from the momentum equations that are used in the CB reconstruction [3]. The inviscid mixing layer computations showed that the difference between hybrid and conservative CB schemes in terms of multigrid cycles is smaller in this case than in the diffusion broadening computations. This indicates that the appearance of the pseudo-compressibility term in the densities (reconstruction) formulas has a stronger effect on the multigrid convergence in the case of viscous problems.

Furthermore, the numerical convergence is also dependent on the intercell interpolation. The computations showed that more multigrid cycles are required when increasing the order of intercell variable interpolation. Since reasonable accuracy for the diffusion broadening problem was obtained by all orders of polynomial interpolation, one may consider the tradeoff between convergence speed and accuracy, especially when dealing with 3-D problems and fine grids. For the diffusion broadening problem the best compromise seems to be achieved by second-order interpolation.

Finally, in [3] we showed that in the limit of constant density incompressible flows the transport CB scheme corresponds to the original characteristics-based scheme for incompressible, constant density flows [7,6], whereas the hybrid and conservative CB schemes lead to a new variant of the CB scheme for incompressible, constant-density flows. The multigrid convergence tests performed in this paper reveal that the conservative CB variant provides the best convergence among the three schemes. This motivates further investigation of the behavior of this scheme for constant-density flows and research in this direction is currently in progress.

Acknowledgement

The financial support from the UK's Engineering and Physical Sciences Research Council (GR/S13668) is greatly acknowledged.

References

- [1] W.J. Rider, D.B. Kothe, E.G. Puckett, I.D. Aleinov, Accurate and robust methods for variable density incompressible flows with discontinuities, in: V. Venkatakrishnan, M.D. Salas, S.R. Chakravarthy (Eds.), *Barriers and Challenges in Computational Fluid Dynamics*, Kluwer Academic Publishers, Boston, MA, 1998, ISBN 0-7923-4855-9, pp. 213–230.
- [2] A.S. Almgren, J.B. Bell, P. Colella, L.H. Howell, M.L. Welcome, A conservative projection method for the variable-density incompressible Navier–Stokes equations, *J. Comput. Phys.* 142 (1998) 1.
- [3] E. Shapiro, D. Drikakis, Artificial compressibility and characteristics-based schemes for variable density, incompressible, multi-species flows: Part I. Derivation of different formulations, *J. Comput. Phys.*, doi:10.1016/j.jcp.2005.05.001.
- [4] A.J. Chorin, A numerical method for solving incompressible viscous flow problems, *J. Comput. Phys.* 2 (1967) 12.
- [5] A. Eberle, Characteristic flux averaging approach to the solution of Euler’s equations, VKI Lecture Series, *Computational Fluid Dynamics* 1987-04, 1987.
- [6] D. Drikakis, P.A. Govatsos, D.E. Papatonis, A characteristic-based method for incompressible flows, *Int. J. Numer. Methods Fluids* 19 (1994) 667.
- [7] D. Drikakis, W. Rider, *High-Resolution Methods for Incompressible and Low-Speed Flows*, Springer-Verlag, Berlin, 2004.
- [8] D. Drikakis, O.P. Iliev, D.P. Vassileva, A nonlinear multigrid method for the three-dimensional incompressible Navier–Stokes Equations, *J. Comput. Phys.* 146 (1998) 301.
- [9] S.-Y. Lin, T.-M. Wu, An adaptive multigrid finite volume scheme for incompressible Navier–Stokes equations, *Int. J. Numer. Methods Fluids* 17 (1993) 687.
- [10] P. Wesseling, *An Introduction to Multigrid Methods*, Wiley, New York, 1991.
- [11] J. Farmer, L. Martinelli, A. Jameson, A fast multigrid method for solving incompressible hydrodynamic problems with free surfaces, AIAA Paper 93-076, 1993.
- [12] Ch. Sheng, L.K. Taylor, D.L. Whitfield, An efficient multigrid acceleration for solving the 3D incompressible Navier–Stokes equations in generalized curvilinear coordinates, AIAA Paper 93-2335, 1993.
- [13] X. Zheng, C. Liao, C. Liu, C.H. Sung, T.T. Huang, Multigrid computation of incompressible flows using two-equation turbulence models: Part 1 – Numerical method, *J. Fluids Eng.* 119 (1997) 893.
- [14] J. Vierendeels, K. Rienslagh, E. Dick, Multigrid semi-implicit line methods for viscous incompressible low mach number flows on high aspect ratio grids, *J. Comput. Phys.* 154 (1999) 310.
- [15] D. Drikakis, O.P. Iliev, D.P. Vassileva, Acceleration of multigrid flow computations through dynamic adaptation of the smoothing procedure, *J. Comput. Phys.* 165 (2000) 566.
- [16] L.D. Dailey, Evaluation of multigrid acceleration for preconditioned time-accurate Navier–Stokes algorithms, *Comput. Fluids* 25 (1996) 791.
- [17] P. Lotstedt, Improved convergence to the steady state of the Euler equations by enhanced wave propagation, *J. Comput. Phys.* 114 (1994) 34.
- [18] J. Steelant, E. Dick, S. Pattijn, Analysis of robust multigrid methods for steady viscous low Mach number flows, *J. Comput. Phys.* 136 (1997) 603.
- [19] D.R. van der Heul, C. Vuik, P. Wesseling, Conservative pressure-correction method for flow at all speeds, *Comput. Fluids* 32 (2003) 1113.
- [20] H. Hisamoto, T. Horiuchi, M. Tokeshi, A. Hibara, T. Kitamori, On-chip integration of neutral ionophore-based ion pair extraction reaction, *Anal. Chem.* 73 (2001) 1382.
- [21] W.E. TeGrotenhuis, R.J. Cameron, M.G. Butcher, P.M. Martin, R.S. Wegeng, Microchannel devices for efficient contacting of liquids in solvent extraction, *Separat. Sci. Technol.* 34 (6) (1999) 951.
- [22] W.E. TeGrotenhuis, R.J. Cameron, V.V. Viswanathan, R.S. Wegeng, Solvent extraction and gas absorption using microchannel contactors, in: W. Ehrfeld (Ed.), *Microreaction Technology: Industrial Prospects*, Springer-Verlag, Berlin, 2000, pp. 541–550.
- [23] B.H. Weigl, P. Yager, Microfluidic diffusion-based separation and detection, *Science* 15 (1999) 346.
- [24] C.N. Baroud, F. Okkels, L. Menetrier, P. Tabeling, Reaction-diffusion dynamics: confrontation between theory and experiment in a microfluidic reactor, *Phys. Rev. E* 63 (2003) 060104(R).
- [25] A. Deshmukh, D. Liepmann, A.P. Pisano, Characterization of a micro-mixing, pumping, and valving system, in: *Proceedings of the 11th International Conference on Solid State Sensors and Actuators (Transducers ’01)*, Munich, Germany, June 10–14, 2001, pp. 950–953.
- [26] P.K. Wong, Y.-K. Lee, C.-M. Ho, Deformation of DNA molecules by hydrodynamic focusing, *J. Fluid Mech.* 497 (2003) 55.
- [27] D. Drikakis, M. Kalweit, Computational modelling of flow and mass transport processes in nanotechnology, in: M. Rieth, W. Schommers (Eds.), *Handbook in Theoretical and Computational Nanotechnology*, American Scientific Publishers, invited chapter, in print, 2004.
- [28] P.J. Kenis, R.F. Ismagilov, G.M. Whitesides, Microfabrication inside capillaries using multiphase laminar flow patterning, *Science* 285 (1999) 83.

- [29] H. Andersson, Microfluidic devices for biotechnology and organic chemical applications, PhD Thesis, Royal Institute of Technology, Stockholm, Sweden, 2001.
- [30] R.F. Ismagilov, A.D. Stock, P.J.A. Kenis, G. Whitesides, Experimental and theoretical scaling laws for transverse diffusive broadening in two-phase laminar flows in microchannels, *Appl. Phys. Lett.* 76 (17) (2000) 2376.
- [31] K.B. Greiner, M. Deshpande, J.R. Gilbert, R.F. Ismagilov, A.D. Stroock, G.M. Whitesides, Design analysis and 3D measurement of diffusive broadening in a Y-Mixer, in: *Technical Proceedings of Micro Total Analysis Systems*, Enschede, The Netherlands, MicroTAS 2000, pp. 87–90.
- [32] A.E. Kamholtz, P. Yager, Theoretical analysis of molecular diffusion in pressure-driven laminar flow in microfluidic channels, *Biophys. J.* 80 (2001) 155.
- [33] A.E. Kamholz, B.H. Weigl, B.A. Finlayson, P. Yager, Quantitative analysis of molecular interaction in a microfluidic channel: the T-sensor, *Anal. Chem.* 71 (1999) 5340.
- [34] M. Engler, N. Kockmann, T. Kiefer, P. Woias, Numerical and experimental investigations on liquid mixing in static micro mixers, *Chem. Eng. J.* 101 (2004) 315.
- [35] P. Gravesen, J. Branebjerg, O.S. Jensen, Microfluidics – a review, *J. Micromech. Microeng.* 3 (1993) 168.
- [36] A. Michalke, On the inviscid instability of the hyperbolic-tangent velocity profile, *J. Fluid Mech.* 19 (1964) 543.
- [37] M. Lesieur, C. Staquet, P.L. Roy, P. Comte, The mixing layer and its coherence examined from the point of view of two-dimensional turbulence, *J. Fluid Mech.* 192 (1988) 511.
- [38] B. Vreman, B. Geurts, H. Kuerten, Discretization error dominance over subgrid terms in Large Eddy Simulation of compressible shear layers in 2D, *Int. J. Numer. Methods Eng.* 10 (1994) 785.
- [39] M.L. Minion, D.L. Brown, Performance of under-resolved two-dimensional incompressible flow simulations II, *J. Comput. Phys.* 138 (1997) 734.
- [40] D. Drikakis, P.K. Smolarkiewicz, On spurious vortical structures, *J. Comput. Phys.* 172 (2001) 309.
- [41] D. Drikakis, Embedded turbulence model in numerical methods for hyperbolic conservation laws, *Int. J. Numer. Methods Fluids* 39 (2002) 763.
- [42] S.G. Yiantsios, B.G. Higgins, Linear stability of plane Poiseuille flow of two superimposed fluids, *Phys. Fluid A* 1 (5) (1989).
- [43] A.F. Ghoniem, G. Heidarnejad, A. Krishnan, Numerical simulation of a reacting shear layer using the transport element method, *AIAA Paper*, 87-1718, 1987.
- [44] A.F. Ghoniem, G. Heidarnejad, A. Krishnan, On mixing, baroclinicity and the effect of strain in a chemically-reacting shear layer, *AIAA Paper* 88-0729, 1988.
- [45] J.N. Renaud, L. Joly, Numerical simulation of variable-density mixing layer, *ESAIM Proc.* 7 (1999) 359.
- [46] M.C. Soteriou, O.M. Knio, A.F. Ghoniem, Manipulation of the growth rate of a variable density, spatially developing mixing layer via external modulation, *AIAA Paper* 91-0081, 1991.
- [47] M.C. Soteriou, A.F. Ghoniem, Effects of the free-stream density ratio on free and forced spatially developing shear layers, *Phys. Fluids A* 7 (8) (1995) 2036.
- [48] E.L. Cussler, *Diffusion, Mass Transfer in Fluid Systems*, Cambridge University Press, New York, 1984.
- [49] E.L. Cussler, *Multicomponent Diffusion*, Elsevier, Amsterdam, 1976.
- [50] C.-W. Shu, S. Osher, Efficient implementation of essentially non-oscillatory shock capturing schemes, *J. Comput. Phys.* 77 (1988) 439.
- [51] P.S. Vassilevski, Preconditioning nonsymmetric and indefinite finite element matrices, *J. Numer. Linear Algebra Appl.* 1 (1992) 59.
- [52] J. Xu, New class of iterative methods for non-self-adjoint or indefinite problems, *SIAM J. Numer. Anal.* 29 (1992) 303.
- [53] J. Xu, A novel two-grid method for semilinear elliptic equations, *SIAM J. Sci. Statist. Comput.* 15 (1994) 231.
- [54] P.K. Newton, E. Meiburg, Particle dynamics in a viscously decaying cats eye: the effect of finite Schmidt numbers, *Phys. Fluids A* 3 (5) (1991).
- [55] A. Ålund, P. Lotstedt, M. Silen, Parallel single and multiple grid solution of industrial compressible flow problems, Number L-0-1 R166 SAAB Military Aircraft Report, AGARD, 1996.
- [56] O. Axelsson, M. Neytcheva, Scalable parallel algorithms in CFD computations, in: M. Hafez, K. Oshima (Eds.), *Computational Fluid Dynamics Review*, 1995, pp. 837–857.
- [57] O. Axelsson, M. Neytcheva, Some basic facts for efficient massively parallel computation, *CWI Quart.* 9 (1996) 9–17.
- [58] A. Brandt, A multilevel adaptive solutions of boundary value problems, *Math. Comput.* 31 (1977) 333.